

https://dspace.org/

Excellent power and cycling stability of Mn2PO4Fbased pseudocapacitor electrode Ceriainduced electronstarvation of surface Mn2 species

Ryan O'connor; Thapelo Mofokeng; Aderemi Haruna; M Terban; Dean Barrett ...

ELSEVIER SCIENCE BV
https://hdl.handle.net/10539/45795
WOS

Downloaded from a DSpace repository. https://dspace.org/

Journal of Power Sources 630 (2025) 236081

Contents lists available at ScienceDirect

Journal of Power Sources

journal homepage: www.elsevier.com/locate/jpowsour

Excellent power and cycling stability of Mn_2PO_4F-based pseudocapacitor electrode: Ceria-induced electron-starvation of surface Mn^{2+} species

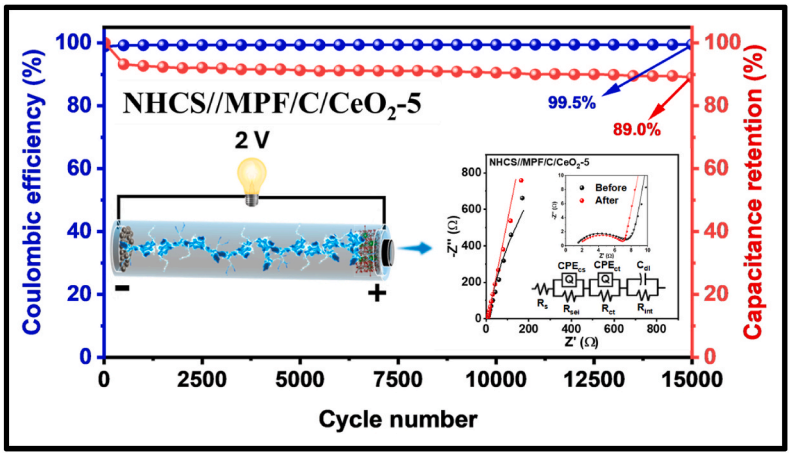
Ryan O'Connor [a], Thapelo P. Mofokeng [a], Aderemi B. Haruna [a], Maxwell W. Terban [b], Dean H. Barrett [a,**], Kenneth I. Ozoemena [a,*]

[a] Molecular Science Institute, School of Chemistry, University of the Witwatersrand, Johannesburg, 2050, South Africa
[b] Max Planck Institute for Solid State Research, Heisenbergstraße 1, 70569, Stuttgart, Germany

HIGHLIGHTS

- Pseudocapacitance of CeO_2-coated Mn_2PO_4F in water-in-salt electrolyte investigated.
- No structural effect on the triplite structure in the presence of CeO_2 or carbon.
- CeO_2 transforms surface Mn^{2+} to Mn^{3+} to enhance the cyclability.
- Asymmetric cell achieved high power and energy densities.
- Pseudocapacitor exhibits excellent cycling stability of 89 % after 15 000 cycles.

GRAPHICAL ABSTRACT



ARTICLE INFO

Keywords:
Manganese fluorophosphate
Triplite
Asymmetric supercapacitor
Hybrid energy storage system
Sodium perchlorate
Water-in-salt electrolyte

ABSTRACT

Manganese fluorophosphate, Mn_2PO_4F (MPF), is investigated as a potential candidate electrode material for aqueous asymmetric supercapacitor systems. CeO_2 coatings at concentrations of different weights are introduced, along with a 10 wt% carbon black (CB) coating serving as a conducting agent. The 5 % CeO_2 (MPF/C/CeO_2-5) composite was identified as a stable, high-power positive electrode material in an asymmetric supercapacitor device using nitrogen-doped hollow carbon spheres (NHCS) as the negative electrode. These electrodes are coupled with a 17 m water-in-salt $NaClO_4$ electrolyte, yielding a sustainable high-power pseudocapacitive device. The device achieves a specific capacitance of 38 F/g, and a maximum energy density of 21.0 Wh/kg at a power density of 390.9 W/kg. Remarkably, at a current density of 3 A/g the device achieved a maximum power density of 11.632 kW/kg at an energy density of 11.2 Wh/kg. Power densities of this magnitude are generally only achieved at higher current densities compared to other manganese-based materials in the recent literature.

* Corresponding author.
** Corresponding author.
E-mail addresses: dean.barrett1@wits.ac.za (D.H. Barrett), Kenneth.ozoemena@wits.ac.za (K.I. Ozoemena).

https://doi.org/10.1016/j.jpowsour.2024.236081
Received 18 September 2024; Received in revised form 30 November 2024; Accepted 14 December 2024
Available online 21 December 2024
0378-7753/© 2024 The Authors. Published by Elsevier B.V. This is an open access article under the CC BY-NC-ND license (http://creativecommons.org/licenses/by-nc-nd/4.0/).

Favourable cycling stability was achieved and attributed to the electronic interaction between CeO_2 and Mn^{2+} as a similar device using pure MPF achieved a capacity retention of only 64.9 % under the same experimental conditions.

1. Introduction

Asymmetric supercapacitors (ASCs) have recently been highlighted as promising candidates for next-generation energy storage systems. While conventional supercapacitors (SCs) use two electrodes of the same material, ASCs use two electrodes of different materials, leading to more flexibility in the design of these devices. For example, the electrodes can consist of an electric double-layer capacitive (EDLC) carbon material which are coated with different functional groups, promoting the Faradaic properties of one electrode while promoting capacitive behavior in the other [1–3]. Alternatively, a battery-type design can be adopted whereby a Faradaic (having bulk redox/ion-intercalation energy storage processes) or pseudocapacitive (having a mix of Faradaic and non-Faradaic energy storage processes) cathode-like (positive) material can be coupled with a carbonaceous EDLC anode-like (negative) material [3–5]. Such systems aim to develop devices with the high-power characteristics of conventional SCs while also providing the high-energy characteristics of conventional battery systems.

Alkali metal fluorophosphates have recently gained attention as promising cathode materials in battery research. These materials utilize highly electronegative polyanionic subunits, along with fluorine, to increase the ionic character of the redox metal species, leading to higher redox potentials in comparison to transition metal oxides commonly used in commercial battery systems [6–8]. Additionally, these materials typically comprise earth-abundant metals, such as Fe, Mn, and V, and are often noted to display redox chemistry through multiple electron reactions [9–11]. Some fluorophosphates, such as $LiVPO_4F$, have competed well in terms of energy density with commercial cathode materials used in Li-ion batteries [10], and have thus been explored as potentially safer, more environmentally friendly, and low-cost alternatives to such materials. Despite the successful implementation of these materials in battery systems, few studies have explored their potential in other electrochemical systems, such as SCs and ASCs. In this study, manganese fluorophosphate (MPF) is investigated as a potential candidate for use as a positive electrode material in an ASC system. Despite its first reporting by Rea and Kostiner (1972) [12] more than four decades ago, MPF remains widely unexplored for electrochemical applications in comparison to other fluorophosphate members. Given the successful use of Mn-based materials in energy storage systems [13,14] MPF should be explored as a candidate for use in supercapacitors and battery systems, particularly in regions like South Africa, which are thought to hold 80 % of global manganese reserves [15].

Recently, Nzimande et al. (2021) reported MPF as a viable cathode material for a reversible aqueous Na-ion battery system [16], and to the best of our knowledge, this is the only report which explores the electrochemical properties of MPF. In their report, a ceria(CeO_2)-coated MPF coupled with a zinc foil anode in an aqueous Na electrolyte produced a device with an average voltage of 1.6 V and a specific capacity of ~195 mAh/g. This demonstration successfully suggests that MPF is a safe, cost-effective, and environment-friendly material that should be further explored for advanced energy storage solutions. In particular, the energy storage mechanisms evident in MPF can be better understood as the study of the material is still in its early stages. Nzimande et al. (2021) further proposed that the CeO_2 coating was particularly important for enabling the electrochemical properties of MPF. CeO_2 coatings promote the structural stability of materials by acting as a protective layer to prevent electrode degradation from processes such as ion-diffusion, electrolyte infiltration, and corrosion in aggressive electrolyte environments [17–19]. Additionally, the reversible oxygen storage properties and catalytic activity of CeO_2 facilitate redox processes and reaction kinetics at electrode interfaces in electrochemical materials leading to improved electrochemical performance [19–22]. Furthermore, the ionic conductivity of CeO_2 promotes the charge-transfer kinetics of electrochemically active materials to ensure the maximum utilization of the active material while enhancing the rate capability, which, coupled with improved structural stability, can greatly benefit high-power electrochemical systems with fast charging/discharging rates [18,23].

Aside from the choice of electrode materials and methods of modifying them to optimize performance, it is also important to consider the choice of electrolyte when designing ASC systems. Concentrated WIS electrolytes have been proven to enhance the operational stability of batteries and supercapacitors, enabling them to withstand higher voltages without the promotion of unwanted side-reactions [24,25]. Expanding the stability window of these devices not only improves their overall performance, safety, and longevity, but also serves as a cost-effective and sustainable alternative to commonly used organic electrolytes. Furthermore, WIS electrolytes offer improved ionic conductivity and have the potential for higher energy densities than salt-in-water aqueous electrolytes.

In this study, a CeO_2-coated MPF was synthesised using a cost-effective microwave-assisted method. This material was used as a positive electrode in an ASC setup coupled with a nitrogen-doped hollow carbon sphere (NHCS) negative electrode in an aqueous water-in-salt (WIS) $NaClO_4$ electrolyte. CeO_2 is used as a coating agent owing to its proven benefits in energy-storage electrode materials. To further the work done by Nzimande et al. (2021), the effect of varying the amount of CeO_2 is investigated to better understand its effect on the electrochemical properties of pristine MPF and to determine whether further additions CeO_2 may prove useful in further optimizing the material's performance. Additionally, 10 wt% carbon black (CB) is added to promote the conductivity of the resulting composites. For the negative electrode, NHCSs were synthesised because they are carbonaceous materials with high surface areas, similar to other EDLC-type materials used for similar applications. The choice of a WIS electrolyte is to expand the stable operating window of the resulting ASC device. To our knowledge, this work is one of the few instances where a fluorophosphate material has been reported as a candidate material for use in ASC systems [26]. It is with this knowledge that this study aims to further define the electrochemical characteristics of MPF and contribute to ongoing studies of fluorophosphates as electrochemical energy materials in systems outside of Li-ion batteries in which they currently predominate.

2. Experimental

2.1. Materials

Lithium fluoride (LiF, ≥99.99 %, Merck), ammonium dihydrogen phosphate ($NH_4H_2PO_4$, ≥98 %, Sigma-Aldrich), manganese nitrate tetrahydrate ($Mn(NO_3)_2•4H_2O$, ≥97.0 %, Sigma-Aldrich), cerium nitrate hexahydrate ($Ce(NO_3)_3•6H_2O$, 99 %, Sigma-Aldrich), potassium hydroxide (KOH, 85 %, ACE Chemicals), carbon black (CB, TIMICAL SUPER C45, MTI Corp.), ethanol (EtOH, ≥99.9 %, Merck), polyvinylidene fluoride (PVDF, $-(C_2H_2F_2)_n-$, HSV900, MTI Corp.), sodium perchlorate ($NaClO_4$, ≥98.0 %, Sigma-Aldrich), N-methyl-2-pyrrolidone (NMP, C_5H_9NO, 99.5 %, Sigma-Aldrich), tetraethyl orthosilicate (TEOS, $Si(OC_2H_5)_4$, 99.999 %, Sigma Aldrich), ammonia solution (25 %, Fluka), resorcinol (C_6H_4-1,3-$(OH)_2$, ≥99 %, Merck), formaldehyde (CH_2O, 37 %, Sigma-Aldrich), and cetyltrimethylammonium bromide (CTAB, $CH_3(CH_2)_{15}N(Br)(CH_3)_3$, ≥98 %, Sigma-Aldrich) were used as

purchased from their respective suppliers. Carbon paper and nickel foam were also used for the electrochemical investigations.

2.2. Preparation of pristine Mn_2PO_4F (MPF) and MPF/C/CeO_2

The synthesis of pristine MPF and the MPF/C/CeO_2 composites follows an established method reported previously [16], however, some alterations were made for this work. For the synthesis of pristine MPF, LiF is used as a fluorine source instead of NaF due to the greater availability of the former precursor. For the synthesis of the MPF/C/CeO_2 composites, rather than only 2 % CeO_2, composites comprising 2.5 %, 5 %, and 7.5 % CeO_2, were produced. Detailed descriptions and schematic representations of the full synthesis procedures are provided in the supplementary text (See Fig. S1).

2.3. Preparation of NHCS

In a sealable glass vessel, tetraethyl orthosilicate (50 mL), ethanol (390 mL) and deionized water (50 mL) were combined and magnetically stirred. Then, 20 mL of 25 % ammonia solution was added, and the vessel was sealed. The clear solution gradually turned milky-white after being left for some time. The solution was then stirred for 12 h and the silica product was collected using a centrifuge. The product was then dried in an oven at 60 °C for 12 h. Next, 2 g of the prepared silica template was added to a solution housed in a sealable vessel containing 140 mL ethanol, 30 mL deionized water, 0.9 g resorcinol, 0.9 mL formaldehyde, and 1 g CTAB. This mixture was stirred with a magnetic stirrer and 10 mL of 25 % ammonia solution was added. The vessel was then sealed before the solution was stirred for 12 h. The white solution gradually turned a light brown colour as the resorcinol formaldehyde (RF) layer formed over the silica template. The obtained light-brown solution was then vacuum filtered and dried in an oven at 60 °C for 12 h. The fine brown powder obtained was then mixed with melamine as a nitrogen source and the mixture was finely ground using a mortar and pestle. The resulting powder was subsequently heated in a tube furnace at 900 °C for 2 h at a heating rate of 10 °C/min under Ar, which resulted in the carbonization of the RF layer. The obtained black powder was then added to a sealable vessel containing 400 mL of deionized water and was then stirred with a magnetic stirrer. Hydrofluoric acid (HF) (20 mL) was then added and the solution was then stirred lightly for 12 h. This allowed the silica template housed in the carbon spheres to be leached without damaging their shells. The solution was then vacuum filtered and dried in a 60 °C oven for 12 h. The product collected was denoted NHCS.

2.4. Characterization

2.4.1. Materials characterization

The materials were characterized using high-resolution transmission electron microscopy (HR-TEM) in a JEOL JEM 2100 at an accelerating voltage of 200 kV with a Thermo Fischer detector for EDS measurements. The samples were dissolved in ethanol, sonicated for approximately 20 min, and dispersed on a carbon-coated copper grid before analysis. High-resolution scanning electron microscopy (HR-SEM) was performed using a Zeiss Auriga Field Emissions SEM running with SmartSEM software and an Oxford X-max detector running with Aztec software for EDX measurements. The samples were stuck on double-sided carbon tape and coated with carbon using an Epitech Carbon Coater on a stage that was inserted into the microscope. Brunauer-Emmett-Teller (BET) analysis was performed using N_2 adsorption in a Micrometrics TriStar 2000 surface area and porosity analyzer. Thermogravimetric analysis (TGA) with weight loss derivative outputs (DTG) was performed using a PerkinElmer 6000 thermogravimetric analyzer. X-ray photoelectron spectroscopy (XPS) analysis was performed using a Thermo ESCAlab 250Xi X-ray photoelectron spectrometer with a monochromatic Al Kα (1486.7 eV) photon sources.

Synchrotron powder X-ray diffraction was measured at the Brockhouse lower-energy wiggler beamline at the Canadian Light Source (CLS), with an incident energy of 15.1 keV, with samples loaded in capillaries that were spun during the measurements for sample improved statistics. A Mythen 1K linear detector mounted onto a Huber diffractometer 2θ arm was used to collect the diffracted beam. The detector acquisitions from the 1K Mythen cover the 2θ range from 10 to 80° and were merged into one single PXRD pattern for each sample measurement using a Python routine [27].

Rietveld refinements: Structure refinements of the diffraction data measured at the Brockhouse lower-energy diffraction beamline (CLS) were performed using TOPAS academic v7 [28]. The instrumental profile was determined by refining to the measurement of the NIST 660b LaB_6 standard sample. Multiphase refinements were then performed for the other samples, wherein the lattice parameters by symmetry, isotropic atomic displacement parameter, and scale factor were refined for distinct phases. Peak broadening due to domain size was accounted for by Gaussian and Lorentzian convolutions, and the strain was modelled using the Stephens model for cubic or hexagonal structures. The background was modelled using Chebychev polynomials with six to eight terms.

Pair distribution function (PDF) analysis: High-Q total scattering data were collected in capillary transmission geometry at the European Synchrotron and Radiation Facility (ESRF) at beamline ID11 experimental hutch 1 with a 2D Frelon camera and an incident wavelength of 0.1653 Å. Energy calibration was performed using Ni and CeO_2 reference material at seven sample-to-detector distances. The samples were then loaded into Kapton capillaries. The total scattering data were background subtracted, normalised, and Fourier transformed to the pair distribution function (PDF) using the software PDFgetX3 within the xPDFsuite [29,30] and structure refinements were performed using PDFgui [31]. Additional total scattering methodology is provided in the Supplementary Information.

2.4.2. Electrochemical characterization

The electrochemical properties of the synthesised materials were first investigated in three-electrode (half-cell) systems. The electrodes were prepared by crushing the active materials with poly(vinylidene fluoride) (PVDF) as a binding agent in a mortar and pestle at a weight ratio of 90:10 until a homogeneous mixture was formed. A few millilitres of N-methyl-2-pyrrolidone (NMP) were then added to the solid mixture to form a viscous slurry which was stirred for 30 min. The slurry was then uniformly dispersed onto a carbon paper disk (A = 0.7854 cm^2, 0.1 mm thickness) through dropwise addition using a glass Pasteur pipette, followed by drying in a 60 °C oven for 12 h to ensure total evaporation of the solvent. The mass loadings of the electrodes were in the range of 1.0–1.2 mg/cm^2. The produced electrodes were used as working electrodes, and a nickel foam disk was used as the counter electrode. Owing to the use of highly concentrated electrolytes and uncertainty regarding the optimal operating conditions of the materials studied, concerns have arisen regarding the choice of an appropriate reference electrode. Thus, carbon paper was chosen as a quasi-reference electrode in these setups. Porous carbon electrodes are typically chemically inert and exhibit excellent stability with minimal potential drift in both aqueous and non-aqueous systems [32,33]. Therefore, carbon paper is expected to maintain reliable reference potentials without the risk of reacting with highly concentrated electrolytes. Hence, it was deemed to be a suitable reference electrode for the study of these materials. The systems were assembled in a Swagelok T-type electrochemical cell, making using a 17 m $NaClO_4$ WIS solution as the electrolyte and glass microfiber filters (Whatman GF/F) as the separator between the electrodes. To ensure optimal conditions, the electrolyte was sonicated at 50 °C for ~30 min before assembly to dissolve any crystal formations and mitigate recrystallization during assembly and experiments. The electrodes and separator disks were soaked briefly in the electrolyte solution before cell assembly, ensuring that the cell was

well-sealed to prevent crystallization of the electrolyte. Cyclic voltammetry (CV), galvanostatic charge-discharge (GCD), and electrochemical impedance spectroscopy (EIS) measurements were performed using a Bio-logic SP300 Potentiostat running on EC-lab software. EIS measurements were conducted using an AC voltage in the frequency range of 0.1 Hz–100 kHz. The specific capacitance, C_s (F/g) of the electrodes was determined using the GCD curves and calculated using Eq (1)) [34]:

$$C_s = \frac{\int I \bullet dt}{\Delta V \times m} \quad [1]$$

where I (A) is the applied current, t (s) is the discharge time, ΔV is the potential window, and m (g) is the active mass of the material coated on the electrode.

For two-electrode investigations, devices were assembled in a coin cell (size 2032) assembly using a 17 m $NaClO_4$ WIS solution as the electrolyte and glass microfiber filters (Whatman GF/F) as the separator between electrodes. MPF/C/CeO_2-coated carbon paper disks served as positive electrodes whereas the NHCS-coated disks served as negative electrodes in the ASC device. Electrodes were prepared using the same method as that described for the three-electrode studies, however, the mass loadings were determined by charge balance calculations. Charge balancing was performed by obtaining the ideal mass ratio of the cathode material to the anode material (from three-electrode investigations) using Eq (2)) – 4)[1,35].

$$q^{+/-} = C_s{}^{+/-} \times m^{+/-} \times \Delta V^{+/-} \quad [2]$$

$$q^{+} = q^{-} \quad [3]$$

$$\frac{m^{+}}{m^{-}} = \frac{C_s{}^{-} \times \Delta V^{-}}{C_s{}^{+} \times \Delta V^{+}} \quad [4]$$

where q^+, m^+, c^+, and ΔV^+ correspond to the charge, mass, specific capacitance, and potential window of the cathode respectively, and q^-, m^-, c^-, and ΔV^- correspond to the charge, mass, specific capacitance, and potential window of the anode respectively. The specific capacitance of the two-electrode system was calculated using Eq (5)).

$$C_s = \frac{4 \int I \bullet dt}{\Delta V \times m} \quad [5]$$

As was the case for eq (1), I (A) is the applied current, t (s) is the discharge time, and ΔV is the potential window; however, m (g) in this case is the combined active mass of the materials coated on both the cathode and the anode. The specific energy (E_s, Wh/kg) and specific power (P_s, W/kg) were calculated from the GCD curves of the two-electrode systems using Eq (6)) and 7) [1,35].

$$E_s = \frac{C_s \times \Delta V^2}{2 \times 3.6} \quad [6]$$

$$P_s = \frac{E_s \times 3600}{\Delta t} \quad [7]$$

where C_s is the specific capacitance of the two-electrode cell calculated from eq (5)), and Δt is the discharge time.

3. Results and discussion

3.1. Physical characterization

3.1.1. S-PXRD

The triplite-type structure of the pristine MPF was identified using $Mn_2(PO_4)F$ (PDF Card – 01-083-6369) with a monoclinic unit cell and space group symmetry *C2/c*. Small impurity peaks were observed and partially identified as $LiMnPO_4$ (LMP) (PDF Card – 00-065-0255) with an orthorhombic unit cell and space group symmetry *Pnma*. A small minority of additional peaks could not be identified via search-matching using the ICDD database. Rietveld refinement was performed for each dataset as shown in Fig. 1a and Figs. S2–S5.

The presence of peak shoulders appearing with $LiMnPO_4$ (Fig. S2) indicates a related phase; however, this cannot be proven with high certainty. Several other isolated peaks were also identified. The unidentified peaks only accounted for approximately 2 % of the area of the diffraction peaks after background subtraction. To stabilize the refinement of the LMP phase, fixed Lorentzian broadening was used to describe the peak shape. A two-phase Rietveld refinement (Fig. S2) was then performed to optimize the lattice parameters, scale factors, and isotropic atomic displacement parameters (one Biso for all atoms in LMP and two for MPF – Biso(Mn) and Biso(P=O=F)). The peak shape for MPF was described using Pseudovoigt convolutions for both the crystallite size and strain broadening. The refinement resulted in a ratio of approximately 6:1 MPF:LMP with MPF lattice parameters of a = 13.41600(4) Å, b = 6.51154(2) Å, c = 10.10601(4) Å, and β = 119.9802 (2)°, and a crystallite size of approximately 260(28) nm (where we estimated the standard deviation from the refinement by multiplying by a factor of 10). Real-space refinement to the PDF determined from total scattering measurement of the same sample gave a consistent result and further gave no indication of a significant contribution from the unknown impurities in the local structure (Fig. S2). Reasonable fits could be achieved as described above, with all defined parameters fixed for MPF to those from the published structure, delta 1 for correlated motion, spherical domain damping, and positions of Mn and F refined by symmetry.

Further Rietveld refinements were performed on the samples with 2.5 %, 5 %, and 7.5 % CeO_2 with 10 % carbon black added (Figs. S3–S5), as well as PDF refinements for the corresponding samples with 2.5 % and 7.5 % CeO_2 as shown in Fig. 1b. In the former case, a significant amount of additional diffuse scattering could be observed close to the baseline, which could be distinctly indexed to the Fm-3m structure of CeO_2, a three-phase refinement was performed. PDF refinements were also performed, including the CeO_2 phase, as the peaks from the nanodomains of CeO_2 could be distinctly observed, confirming that the coherence length is only on the order of 1–2 nm. We did not observe significant changes in the lattice parameters of MPF between the samples, indicating that the presence of CeO_2 and CB does not strongly influence the structure of MPF. A PXRD pattern was also obtained for the NHCS negative electrode material and is presented in Fig. S7.

3.1.2. XPS analysis

XPS analysis was performed to further investigate the surface chemistry and elemental composition of the materials, and the results are summarized in Fig. 2. The survey spectra (Fig. S17a) and elemental compositions (see Table S2) obtained from this analysis display all the expected elements at their typical binding energies. An asymmetric peak centered at ~647 eV was observed for the pristine MPF and composite samples corresponding to Mn 2p (Fig. 2a). The peak located at ~641.6 eV (dotted line), corresponding to the Mn $2p_{3/2}$ state, was deconvoluted into three peaks corresponding to the presence of both Mn^{2+} (~641.1 eV) and Mn^{3+} species (~642.5 eV), along with a satellite peak commonly seen for Mn^{2+} species (~645.0 eV) [36]. A peak corresponding to the Mn $2p_{1/2}$ state was also observed at ~653.5 eV for both pristine MPF and the composite samples, which was deconvoluted into two peaks corresponding to Mn^{2+} (~653.0 eV) and Mn^{3+} (~654.5 eV) species [36]. The spin-orbit splitting between the Mn $2p_{3/2}$ and Mn $2p_{1/2}$ was found to be ~12.0 eV for pristine MPF, with a slight decrease in the splitting observed for the composite samples (~11.8 eV). This slight decrease in spin-orbit splitting for the composite samples suggests partial oxidation of surface Mn species, resulting from the addition of the CeO_2 coatings.

To further investigate the extent of this oxidation between samples, the deconvoluted peak areas were calculated to determine the ratio of Mn^{2+} to Mn^{3+} species. According to the given deconvolution, pristine MPF consists of ~63.9 % Mn^{2+} and ~36.1 % Mn^{3+}, MPF/C/CeO_2-2.5

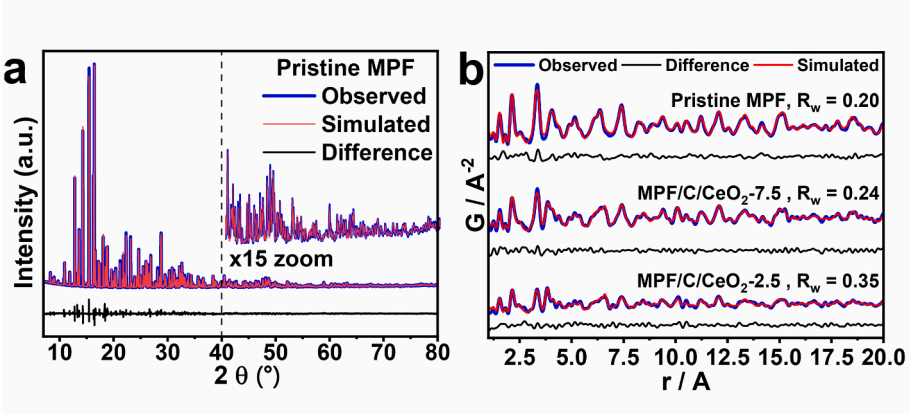


Fig. 1. a) Rietveld refinement fitting of pristine MPF with the higher angle region from 42 to 80° 2θ magnified, showing a good quality fit of the data to high angles to the structure refinement model (Similar plots for the other sample compositions are given in the SI), and b) PDF fittings for pristine MPF, MPF/C/CeO_2-2.5, and MPF/C/CeO_2-7.5.

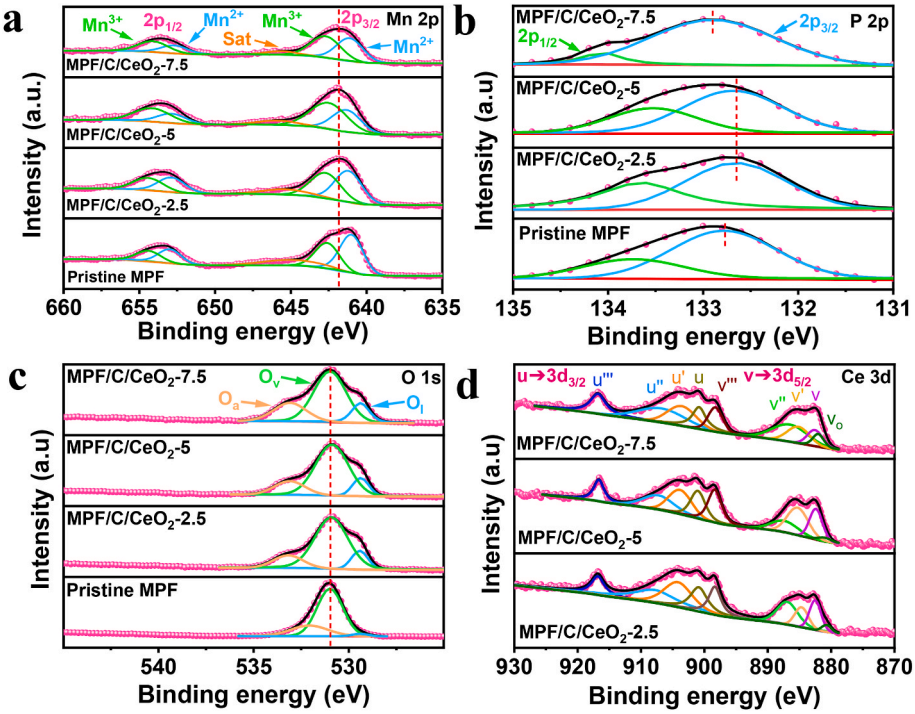


Fig. 2. XPS spectra illustrating deconvoluted a) Mn 2p, b) P 2p, and c) O 1s peaks for the pristine MPF and MPF/C/CeO_2 composites; and deconvoluted d) Ce 3d peaks for the MPF/C/CeO_2 composites.

consists of ~56.7 % Mn^{2+} and ~43.3 % Mn^{3+}, MPF/C/CeO_2-5 consists of ~53.5 % Mn^{2+} and ~46.5 % Mn^{3+}, and MPF/C/CeO_2-7.5 consists of ~49.1 % Mn^{2+} and ~50.9 % Mn^{3+}. This result showcases that the increased addition of CeO_2 results in a decrease of surface Mn^{2+} species, attributed to increased oxidizing ability with a greater presence of CeO_2. Furthermore, this result corroborates EDX data where Ce was observed to show a preferential interaction with Mn. The varying presence of Mn^{2+} and Mn^{3+} species in the samples is of particular interest to understand for further electrochemical analysis of these samples. Generally, Mn^{3+} species are noted to be more electrochemically active than Mn^{2+}, however, concerns over the unfavourable effects of Jahn-Teller distortion and disproportionation reactions associated with Mn^{3+} often result in lower stability, yet Mn^{2+} dissolution may also be a notable challenge in other systems [37–40]. Interestingly, however, Roy et al. (2024) used DFT calculations to show how introducing Jahn-Teller distortion in tungsten oxide through the introduction of interlayer water enhances the electrochromic performance, structural stability, and cyclability of the material [41]. Furthermore, Lv et al. (2022) have highlighted that disproportionation reactions can be beneficial for some applications, whereby they highlighted that reversible MnO_2/Mn^{2+} transitions were enabled through disproportionation of Mn^{3+}species in a Zn-MnO_2 hybrid battery system [42]. Such studies highlight the unique complexities associated with Mn-based materials and showcase how the nature of Mn species present can play a significant role in the electrochemical and physical properties of the materials. Depending on the system involved, the overall performance of the materials can vary significantly based on the content of Mn species present. In some cases, species which may be viewed as less favourable in one application may prove more beneficial in another. Further analysis of the Mn species present in pristine MPF and the CeO_2 composites, perhaps through the use of DFT calculations, would assist in investigating whether effects such as Jahn-Teller distortion or disproportionation reactions play a role

in the performance and stability of the materials. This information may provide insight into optimizing the amount of CeO_2 added to bring about the most beneficial performance of the materials. With this in mind, Mn XPS data suggests that the nature of Mn species is significantly affected by the addition of varying CeO_2 coatings. The amount of CeO_2 added plays a role in varying the overall composition of Mn^{2+} and Mn^{3+} species which are expected to effect the stability and electrochemical performance of the materials.

The P 2p peak (Fig. 2b), located between 131.2 and 134.9 eV, is in the typical region expected for phosphate species. For all samples investigated this peak was deconvoluted to two peaks corresponding to the P $2p_{1/2}$ (~133.8 eV) and P $2p_{3/2}$ (~132.7 eV) states, with the former corresponding to the presence of metal-phosphorus bonds and the latter corresponding to oxidized phosphorus and surface phosphate groups [43]. A slight reductive shift (~0.1 ev, dotted lines) is observed with the addition of 2.5 % and 5 % CeO_2, which then reverses with further addition to 7.5 % CeO_2. This suggests that with additions of CeO_2 up to 5 %, P species also contribute to the oxidation of Mn species. It is possible that P species begin to experience an increased binding affinity to Mn as the CeO_2 coatings oxidize the surface of pristine MPF, leading to the observed reductive shift. Further addition of CeO_2 to 7.5 % leads to an oversaturation effect whereby P species also begin to oxidize at the surface of pristine MPF which may compromise the substrates' chemical stability.

The O 1s peak centered around ~531.0 eV (Fig. 2c, dotted line) was deconvoluted into three peaks for all samples analyzed. Peak O_a (~532.1 eV for PMPF and ~533.2 eV for the CeO_2 composites) is attributed to the presence of adventitious oxygen species, while O_l (~529.4 eV) corresponds to the presence metal-oxide lattice species [44]. Notably, the intensity of the O_l peak was significantly more pronounced in the CeO_2 composites than in the pristine MPF because of the increased metal oxide bonds contributed by the CeO_2 coating on the surface of the pristine MPF substrate. The peak O_v, centred at ~531.0 eV, traditionally corresponds to oxygen vacancies, however, recent debate questions the accuracy of this assignment. Frankcombe and Liu suggested that this results from chemisorbed water or oxygen atoms that have been passivated with absorbed hydrogen on the material surface [45]. With this in mind, deconvoluted peak areas suggest the composition of peak O_v in the samples are as follows: pristine MPF consists of ~73.4 %, MPF/C/CeO_2-2.5 consists of ~71.9 %, MPF/C/CeO_2-5 consists of ~70.8 %, and MPF/C/CeO_2-7.5 consists of ~62.7 %. These percentages are quite high if it is assumed to arise from oxygen vacancies, and as such it is more reasonable to assume that these signals may arise from chemisorbed water or passivated oxygen. However, if we assume a partial contribution to this signal arises from oxygen vacancies, or perhaps oxygen deficient regions, the percentage composition of O_v species would suggest that increasing additions of CeO_2 results in a decrease in the presence of these species. Oxygen vacancies have been observed to enhance electrochemical performance of some materials, however, particularly when the presence of such species is quite large it can lead to structural instability and thus electrode degradation in electrochemical systems [46,47]. Chen et al. (2023) have also explored the effect of NaOH addition on the morphology, structure, and electrochemical performance of $LiMn_2O_4$ cathodes [48]. The authors found that NaOH addition significantly affects the content of Mn^{3+} and oxygen vacancies, and attributed higher overall electrochemical performance to synergistic interactions between these species, particularly at higher Mn^{3+} contents. The variation in the overall presence of oxygen vacancies is thus expected to effect the performance of the as-synthesised materials, however, it is important to better understand the species present which may be contributing to the O_v signal. To further investigate the possible contributions to this signal, DFT calculations would need to be employed to better elucidate the electronic structure of the material, particularly when considering the possibility of oxygen vacancies. Nevertheless, O 1s XPS confirmed the presence of metal oxide bonding between the Mn, O/Ce, and O species in the materials studied.

A very weak F 1s (Fig. S17b) peak was also evident at ~684.3 eV in all the samples studied which is the region typical of metal fluorides [49]. It could also be argued that a slight reductive shift is evident in the F 1s spectra with further additions of CeO_2, which again suggests the CeO_2 coatings alter the nature of chemical bonds present in pristine MPF. Given that the F 1s signals are relatively weak, this observation should be interpreted with caution as it may lack reliability. The intensity of the CeO_2-coated composites decreased and shifted slightly (~0.5 eV) towards lower binding energies. Fluorine is expected to be present predominantly in the bulk of the pristine MPF and thus is not expected to be present in high concentrations on the surface, which accounts for the low intensity of this signal. The further decrease in the intensity of this signal for the CeO_2 composites is attributed to the masking of the pristine MPF by the CeO_2 and carbon black coatings. A slight shift (~0.3–0.5 eV) towards lower binding energies is also evident in the CeO_2 composites which further shows a change in the chemical environment at the surface of the pristine MPF substrate resulting from the addition of CeO_2.

A C 1s peak (Fig. S17c) was observed for the three CeO_2-coated composites in the range of ~282.7–287.4 eV. This peak was deconvoluted into four peaks located at ~284.4 eV, corresponding to the presence of C-C bonds, ~285.0 eV, corresponding to the presence of C-O species, ~287.1 eV, corresponding to the presence of C=O species, and ~288.7 eV, corresponding to the presence of O-C=O species [50]. The C 1s spectra showed no significant changes among the composites, with the signal primarily originating from the presence of carbon black, suggesting that the carbon black coating did not undergo any chemical alteration in the presence of pristine MPF or CeO_2.

Fig. 2d shows the Ce 3d spectra for each CeO_2 composite, with three distinct peaks centered at ~884.4, 902.3, and 916.7 eV. While the well-defined peak at 916.7 eV is a common indicator of the presence of Ce^{4+}, further deconvolution of the other two peaks suggests the coexistence of Ce^{3+} and Ce^{4+} species. As is common practice for Ce 3d XPS analysis, the doublet peaks corresponding to Ce $3d_{3/2}$ and Ce $3d_{5/2}$ states are denoted as u and v, respectively. Peaks assigned to Ce^{4+} include v (882.6 eV), v'' (887.0 eV), v''' (898.4 eV), u'' (907.7 eV), and u''' (916.7 eV). Similarly, the peaks assigned to Ce^{3+} include v_o (881.4 eV), v' (885.0 eV), u_o (900.9 eV), and u' (904.1 eV) [51,52]. It should be noted that the deconvolution of Ce 3d spectra is a notable challenge, particularly when mixed-valence species are involved. Notably, in the deconvolution provided here, there is a missing peak u which is expected in the region of 900–901 eV, however, it was decided to provide the given deconvolution as it was the most consistent among the composites studied. Discrepancies in the binding energies for some of these peaks are expected to result from the complex nature of the chemical environment of the Ce species. Interactions between CeO_2 and the pristine MPF substrate likely play a role in the identity of Ce species, especially given the changes noted in the chemical environment of Mn species with variation in the loading of CeO_2. Furthermore, given that XPS is a surface-based characterization method, increased additions of CeO_2 and the addition of 10 % carbon black is expected to mask pristine MPF and thus may not reliably represent the surface chemistry evident on the substrate. As such, the interpretation of this data should be approached with some caution. It is also noted that further analysis of this data through the use of DFT calculations would greatly assist in understanding the nature of the elemental species present in the materials, particularly in the case of Mn and O species which are expected to play a significant role in the electrochemical performance of the materials. Nethertheless, XPS analysis concluded that the surface chemistry of the materials involved is greatly determined by the interplay between the CeO_2 coating and the pristine MPF substrate, which is expected to play a vital role in the electrochemical performance of the materials when surface-controlled kinetics are a major contributor to the overall performance. This result also further suggests preferential interactions are evident between pristine MPF and the CeO_2 coatings as was suggested from microscopy and EDX analyses.

Other characterization methods such as electron microscopy (Figs. S8–12), thermogravimetric analysis (Fig. S14), and N_2 physisorption (Fig. S15) are also provided in the supplementary text. These techniques highlight that the as-synthesised materials retain similar structural and morphological properties to those reported previously [16].

3.2. Electrochemical characterization

3.2.1. Three-electrode investigation

The electrochemical properties of pristine MPF and MPF/C/CeO_2 composites were analyzed using a three-electrode setup with 17 m $NaClO_4$ as the electrolyte. Fig. 3a shows the CV curves of the synthesised materials at 1 mV/s scan rate. All materials operated in a voltage window between 0 and 1.4 V, with double-layer capacitive behaviour in the range of 0–0.6 V and redox activity between 0.6 and 1.4 V suggesting pseudocapacitive energy storage. Improved charge-transfer kinetics were evident in the MPF/C/CeO_2 composites given the shift in the anodic peak potentials (1.25 V for pristine MPF down to ~1.14 V for the MPF/C/CeO_2 composites). The performance of MPF/C/CeO_2-5 was more favourable as compared to the 2.5 % and 7.5 % CeO_2 composites given it achieved the greatest capacitive contribution in the double-layer capacitive region (17.0 F/g, as compared to 8.0 F/g for MPF/C/CeO_2-2.5 and 11.7 F/g for MPF/C/CeO_2-7.5).

GCD data (Fig. 3b) shows that the as-synthesised materials display similar profiles between 0 and 1.4 V, having non-linear curves which again suggest a pseudocapacitive energy storage mechanism. The data suggests that MPF/C/CeO_2-5 and MPF/C/CeO_2-7.5 display comparable performance, having the greatest gravimetric specific capacitances (42.4 F/g for pristine MPF, 40.1 F/g for MPF/C/CeO_2-2.5, 43.6 F/g for MPF/C/CeO_2-5, and 43.8 F/g for MPF/C/CeO_2-7.5) and discharge times. This result, coupled with observations from CV data suggests MPF/C/CeO_2-5 was the most favourable candidate to consider for two-electrode investigations.

EIS is another important technique for analyzing the electrochemical properties of materials. Fig. 3c illustrates the Nyquist plots obtained from the EIS measurements for the samples studied with their respective electrical equivalent circuits (EEC, Fig. 5c, see inset). Nyquist plots were modelled to fit the combined Randels circuit (RC) comprising the solution/electrolyte (R_s), solid-electrolyte interface (R_{sei}), interfacial resistance (R_{int}) resulting from IR drop, charge-transfer resistance (R_{ct}) resulting from electron transport, and double-layer capacitance (C_{dl}). Furthermore, two constant phase elements (CPE) were fitted to the model corresponding to charge-transfer processes (CPE_{ct}) and the solid-electrolyte interface heterogeneity (CPE_{sei}). The impedance of the CPEs correlates to the power law relationship Eq (8)) [53].

$$Z_{CPE} = [Q(j\omega)^{a}]^{-1} \quad [8]$$

where Q represents the frequency-independent constant associated with the interface involved, j = $\sqrt{-1}$, ω represents the radial frequency, and

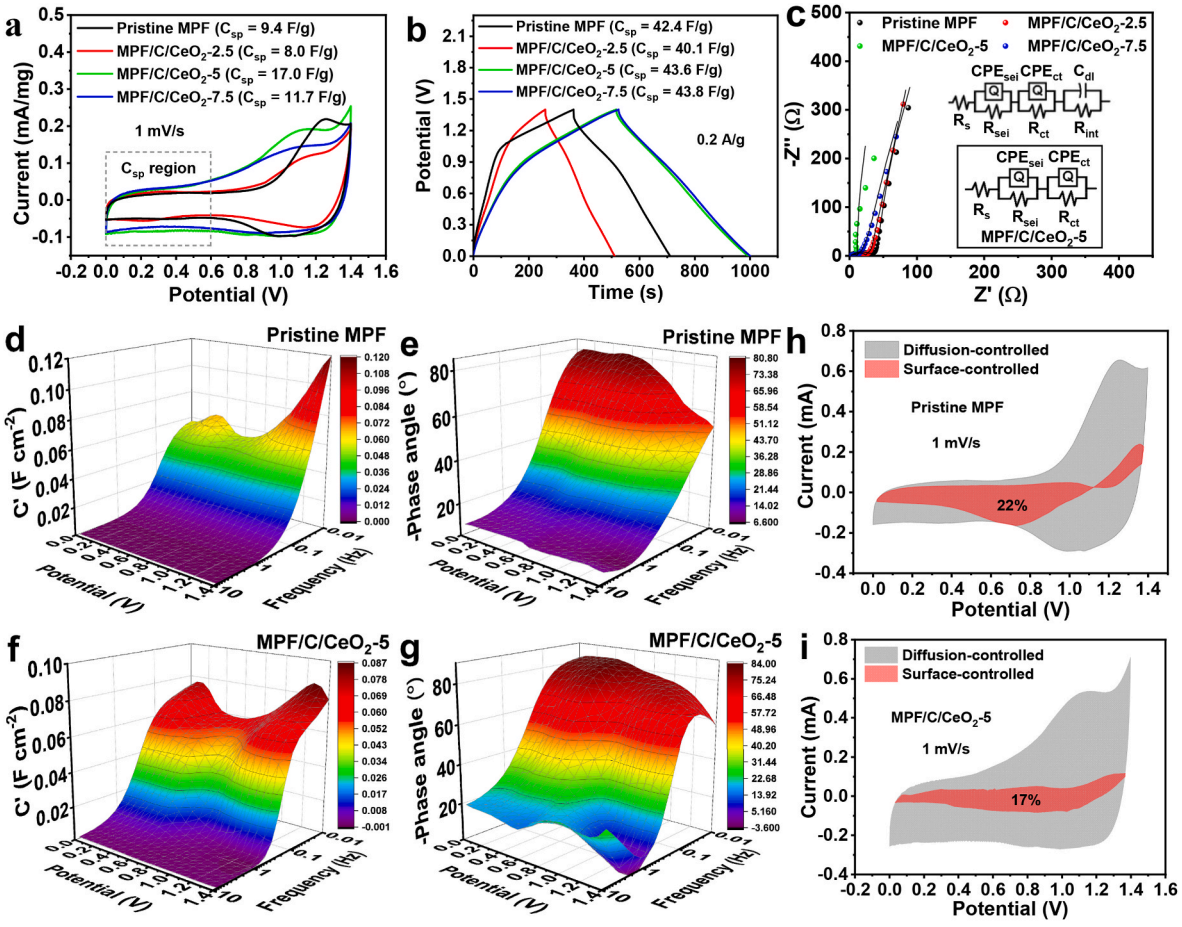


Fig. 3. a) CV curves of pristine MPF and the MPF/C/CeO_2 composites at 1 mV/s scan rates (with specific capacitance contribution in the inset region), b) GCD curves of pristine MPF and the MPF/C/CeO_2 composites at 0.2 A/g current density with calculated specific capacitances, c) Nyquist plots of pristine MPF and the MPF/C/CeO_2 composites (with insets showing the equivalent circuits for MPF/C/CeO_2-5 and the other samples). 3D bode plot representations of d) the real area-normalised capacitance (C′) vs frequency vs voltage and e) phase angle (°) vs frequency vs voltage for Pristine MPF; and c) the real area-normalised capacitance (C′) vs frequency vs voltage and d) phase angle (°) vs frequency vs voltage for MPF/C/CeO_2-5 composite. Coloured bars correspond to the magnitude of C′ and the phase angle (°). Comparison of the capacitive and diffusion-controlled contributions at 1 mV/s in h) pristine MPF and i) MPF/C/CeO_2-5.

the parameter "a" is the slope of log Z vs log F. The value of "a" ranges from $-1 \leq a \leq 1$, whereby a value of $a = 0$ implies purely resistive behaviour, while a value of $a = 1$ implies purely capacitive behaviour, and a value of $a = -1$ implies purely inductive behaviour of the element involved. If $a = 0.5$, the CPE is equivalent to the Warburg impedance (Z_w). Analysis of the Nyquist plots revealed the semi-circle diameter of pristine MPF was the greatest of the materials studied, while the CeO_2 composites exhibited smaller semi-circle sizes indicating a decrease in the charge-transfer resistance. All the materials also displayed a line at an angle of approximately 70° in the low-frequency region, with 5 % CeO_2 having an almost 90° line. Typically, as the angle of this line approaches 90°, it indicates a purely capacitive system [54]. Table S4 summarizes the EIS parameters obtained for the analyzed materials. Notably, MPF/C/CeO_2-5 couldn't be fitted with a double-layer capacitive element or an interfacial resistance in the Randels circuit, suggesting non-ideal behaviour. If we consider series resistance only in terms of $R_s + R_{sei} + R_{ct}$, the series resistance for the materials was found to be 41.43 Ω in PMPF, 34.86 Ω in MPF/C/CeO_2-2.5, 10.87 Ω in MPF/C/CeO_2-5, and 14.30 Ω in MPF/C/CeO_2-7.5. This result suggests that the carbon black and CeO_2 coating leads to an increase in conductivity, with further addition of CeO_2 to 5 %, achieving the best overall conductivity. The CPE_{ct} for all materials obtained an "a" value of 0.8 or greater, suggesting that charge-transfer processes are predominantly capacitive. For CPE_{sei}, all materials possess an "a" value close to 0.5, implying the SEI acts as a resistive component. Given the results from CV, GCD and EIS above, it was decided that it would be best to focus primarily on the MPF/C/CeO_2-5 composite for two-electrode investigations. Three-electrode studies were also conducted on the NHCS anode to perform mass balance calculations for the ASC device, as shown in Fig. S18.

Given the complex nature of the energy-storage mechanisms observed in composite materials, staircase potentio-electrochemical impedance spectroscopy (SPEIS) measurements were performed to provide better insight into the processes involved at varying potentials. 3D Bode plots were generated for pristine MPF and MPF/C/CeO_2-5, with real-area capacitance (C') (Fig. 3d and f, respectively) and the phase angle (°) (Fig. 3e and g, respectively) as dependent variables against the frequency (Hz) and potential (V) [55,56]. From the real capacitance of pristine MPF (Fig. 3d), it is evident that at higher frequencies the system response is not frequency dependent given that the real capacitance remains constant across the entire potential range, suggesting predominantly double-layer capacitive behaviour. At low frequencies, the system response becomes more frequency dependent as seen by the variation in real capacitance over the potential range, suggesting the presence of Faradaic energy storage at higher (1.4 V) and non-Faradaic energy storage at lower (0.28 V) potential extremes. The sharp increase in real capacitance above 1.0 V indicates the presence of fast-moving ionic diffusion processes, while the slight increase at 0.28 V is attributed to capacitive contribution from non-Faradaic processes. In comparison, the real capacitance of MPF/C/CeO_2-5 (Fig. 3f) shows the system is not frequency dependent in the higher and lower potential regions, however, in the mid-potential range (0.6–1.0 V) the system is slightly frequency dependent. This result again suggests a pseudocapacitive energy storage mechanism. The contributions to the real capacitance for MPF/C/CeO_2-5 at 0.1 Hz are of similar magnitude, which contrasts the sharp increase noted for pristine MPF at the higher (1.4 V) potential limit, suggesting some suppression of diffusion-processes resulting from the presence of the CeO_2 and carbon black coatings. In terms of the phase angle, pristine MPF (Fig. 3e) reaches a maximum of ~80° between 0 and 0.6 V at 0.1 Hz, and a minimum of 53.1° at 1.4 V. This suggests EDLC-type behaviour is predominant at lower potentials and the presence of fast-moving ionic diffusion processes at higher potentials. Above ~0.05 Hz, there is a slight frequency dependence between 0.3 and 0.7 V, suggesting pseudocapacitive behaviour in this region. In comparison, MPF/C/CeO_2-5 (Fig. 3g) displays similar behaviour, with the phase angle reaching a maximum of ~83° between 0 and 0.6 V and a minimum of 57.4° at the higher end potential at 0.1 Hz. Also, above ~0.05 Hz a slight frequency dependence in the mid-potential region is observed. This result suggests that both pristine MPF and MPF/C/CeO_2-5 display predominantly capacitive energy storage mechanisms in the lower potential regions, diffusion-controlled energy storage mechanisms at the higher potential regions, and a mixture of these mechanisms in the mid-potential regions. Similar plot shapes were obtained for the 2.5 % CeO_2 and 7.5 % CeO_2 composites (Fig. S19) suggesting a similar charge-storage mechanism for each of the CeO_2 composites.

Given the observed mixture of Faradaic and non-Faradaic processes in the studied materials, it was deemed necessary to attempt to establish which processes predominate in the observed electrochemical behaviour. Therefore, further investigations focused on PMPF and MPF/C/CeO_2-5 to elucidate the dominant energy-storage mechanisms predominating after the addition of CeO_2. From the fundamental concepts of CV and using Dunn's method [57], it is possible to quantify the capacitive (or non-Faradaic) contribution of a system via Eq (9)).

$$i(V) = k_1 v + k_2 v^{1/2} \quad [9]$$

which can be rearranged to Eq (10).

$$i(V) \,/\, v^{1/2} = k_1 v^{1/2} + k_2 \quad [10]$$

where $k_1 v$ represents the capacitive contribution, and $k_2 v^{1/2}$ represents the diffusion contribution. A plot of $i(V)/v^{1/2}$ against $v^{1/2}$ yields a linear plot, where k_1 is the gradient and k_2 is the y-intercept, allowing for the determination of Faradaic and non-Faradaic contributions to the system. Fig. 3h and i illustrate the CV curves of pristine MPF and MPF/C/CeO_2-5 at 1 mV/s, respectively, with their capacitive contributions calculated using Dunn's method highlighted in red. Pristine MPF exhibited a capacitive contribution of 22 %, while the MPF/C/CeO_2-5 composite was 17 %. As the scan rate increased, so too did the capacitive contribution for both pristine MPF and the MPF/C/CeO_2-5 composite (Figs. S20a and S20c, respectively), where at the highest scan rate of 10 mV/s, pristine MPF was noted to have a nearly 50/50 contribution from both diffusional and capacitive processes, whereas for the MPF/C/CeO_2-5 composite, there was a 60/40 diffusional/capacitive split. The result suggests that CeO_2 addition promotes diffusional processes, resulting from an increased number of adsorption/desorption sites. If we use the same fundamentals followed by Dunn's method, it is known that the current response (i/A) of a system is related to the scan rate (v/Vs^{-1}) through the power law relationship expressed in Eq (11)) and 12) [58].

$$i(V) = i_{cap} + i_{diff} = an^b \quad [11]$$

$$\log i(V) = b \log v + \log a \quad [12]$$

where v (mV/s) is the scan rate, and a and b are adjustable parameters, with b equal to the slope of the linear curve log i(V) vs. log (v). The value of b is an indicator of which kinetics predominate in each system, with a value of $b = 1$ indicating that surface-controlled (or non-Faradaic/capacitive) kinetics are predominant while a value of $b = 0.5$, indicating that ionic diffusion-controlled (or Faradaic/redox) kinetics are predominant. A value of b between 0.5 and 1 thus suggests a mixture of both surface-controlled and diffusion-controlled processes (pseudocapacitive behaviour) [59]. Evaluation of the energy-storage mechanisms of these materials yielded b values (Figs. S20b and S20d), ranging from 0.58 to 0.64 for pristine MPF and from 0.62 to 0.72 for the MPF/C/CeO_2-5 composite. This would suggest that a predominantly diffusion-controlled mechanism is expected for pristine MPF, while a predominantly surface-controlled mechanism is expected for the MPF/C/CeO_2-5 composite. This is somewhat contradictory to the trends observed from the CV and histogram plots seen in Fig. 3 and S20; however, the mixed kinetics coupled with the varying morphology of the materials studied warrants some caution regarding the interpretation of

the b value [60,61]. Particularly, in systems where diffusion-controlled and surface-controlled processes both significantly contribute to the storage mechanism, the b value may not reliably identify the predominant mechanism accurately. Nevertheless, for both pristine MPF and the MPF/C/CeO_2-5 composite, the b values range between 0.5 V and 1 V suggesting a pseudocapacitive storage mechanism is evident in the materials.

3.2.2. Asymmetric supercapacitor device

Given that the 5 % CeO_2/CB/MPF composite was selected as the most suitable candidate for further investigation, the ASC device was assembled using 17 m $NaClO_4$ as the electrolyte, the 5 % CeO_2/CB/MPF composite, and NHCS as the positive and negative electrodes respectfully. Using eq. (2)) - 4), charge balancing calculations suggested that the ideal mass loading ratio for the positive and negative electrodes was 1:2. Three-electrode CV measurements of both the positive and negative electrodes (Fig. 4a) at a scan rate of 1 mV/s show a theoretical potential window of approximately 2.5 V, however, the ASC device achieved the most stable window in the range of 0 V–2.0 V, as illustrated in Fig. 4b. Although it was possible to perform CV measurements up to 2.5 V, long-term cycling up to this higher potential led to premature cell failure. Additionally, the GCD curves began to deviate significantly from an ideal charge-discharge shape when cycled above 2 V, which is particularly evident at a very low current density of 0.1 A/g as seen in Fig. 4c. Consequently, the maximum cell voltage was set at 2 V to further analyse the capacitance, energy, and power. The capacitance of the full cell was calculated at current densities between 0.1 A/g – 3.0 A/g as illustrated in Fig. 4d, whereby a maximum specific capacitance of about 37.8 F/g was obtained for NHCS//MPF/C/CeO_2-5.

Cycling stability studies were performed on the NHCS//MPF/C/CeO_2-5 full cell device, as well as the NHCS//pristine MPF device, to further investigate the effect of the CeO_2 coating on the stability of pristine MPF. The CV and GCD data of the NHCS//pristine MPF device are shown in Fig. S21. The devices were cycled between 0 V and 2 V at a current density of 1 A/g for 15 000 cycles as shown in Fig. 5a. Capacity fading was noted in both the ACS devices, predominantly over the first 500 cycles; however, a significantly greater loss in capacitance was observed for the NHCS//pristine MPF device (Fig. 5b). It is interesting to note that despite displaying superior performance in 3-electrode investigations, the NHCS//MPF/C/CeO_2-5 device performed slightly worse in comparison to the NHCS//pristine MPF device. This may be a result of the interaction between the positive and negative electrode in the 2-electrode system, as compared to when the positive electrode performance was measured against Ni foam in 3-electrode investigations. It was observed that pristine MPF displays slightly more surface-controlled kinetics (Fig. 3h) as compared to the MPF/C/CeO_2-5 composite (Fig. 3i).

Particularly in the supercapacitor system, the fast-moving surface-controlled kinetics may contribute significantly to the overall performance of the device, in which charge separation across both the positive and negative electrodes may be more or less favourable depending on the interaction between the electrode materials. The increased surface-controlled kinetics evident in pristine MPF may make it a better suited partner for the NHCS electrode as compared to MPF/C/CeO_2-5, leading to the observed difference in the performance of the NHCS//pristine MPF device compared to the NHCS//MPF/C/CeO_2-5 device. After 15 000 cycles the NHCS//pristine MPF device retained 64.9 % of its initial capacitance (Fig. 5b), whereas the NHCS//MPF/C/CeO_2-5 device retained 89 % (Fig. 5a). This result suggests that the CeO_2 coating significantly contributes to the overall stability of the pristine MPF substrate, perhaps because of the inhibition of diffusion-controlled processes on the pristine MPF surface, or promotion of surface-controlled processes evident on the CeO_2 coating itself, which prevents chemical alterations on the surface of the pristine MPF which may lead to passivation of the electrode. Furthermore, XPS analysis of Mn species (Fig. 2a) highlighted a variation in the presence of Mn^{2+} and Mn^{3+} species between pristine MPF and the CeO_2-coated samples. It is apparent that the composition of these species in MPF/C/CeO_2-5 may be more favourable for promoting overall stability as compared to pristine MPF.

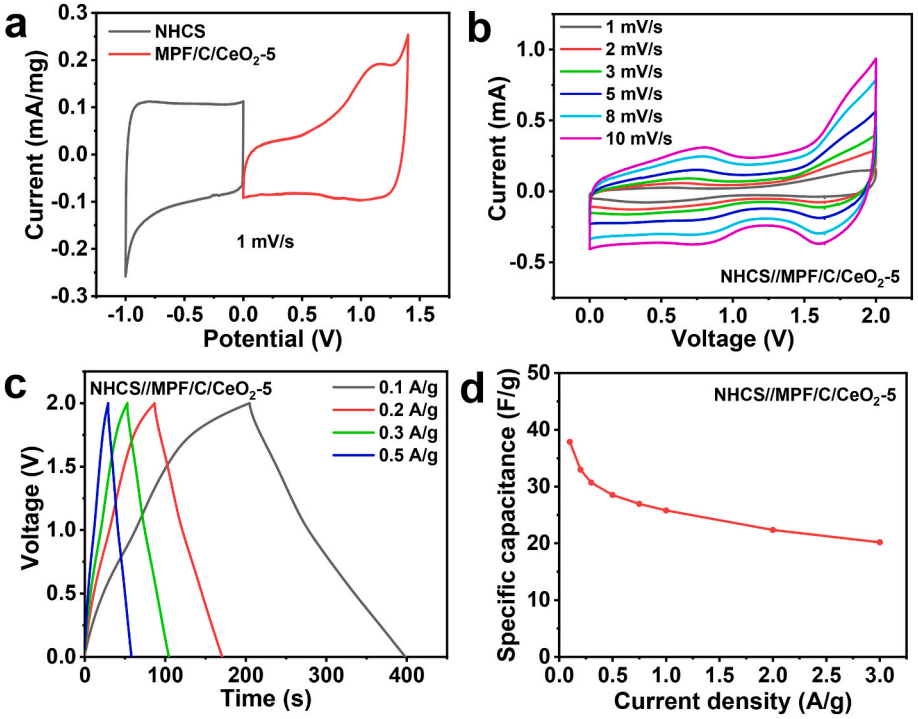


Fig. 4. a) CV curves of NHCS and MPF/C/CeO_2-5 at 1 mV/s, b) CV curves of the NHCS//MPF/C/CeO_2-5 device at scan rates between 1 and 10 mV/s, c) GCD curves of the NHCS//MPF/C/CeO_2-5 device at current densities between 0.1 and 0.5 A/g, d) Specific capacitance versus current density for the NHCS//MPF/C/CeO_2-5 devices.

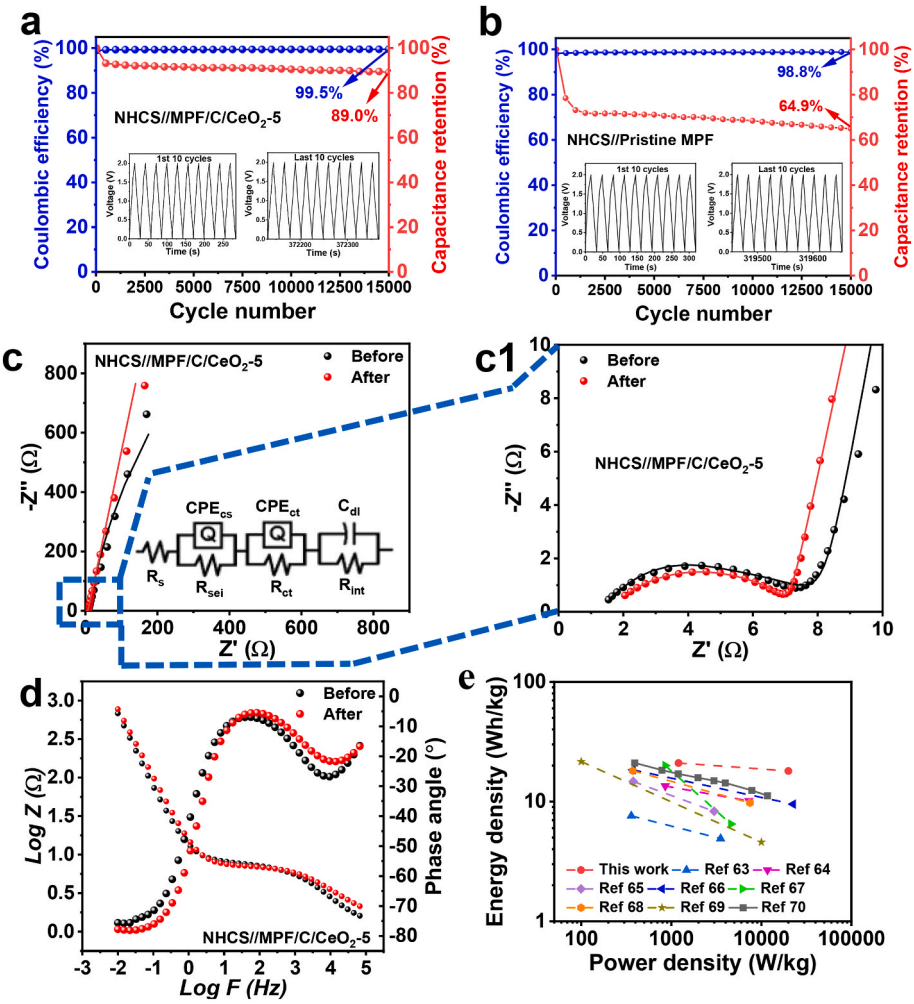


Fig. 5. a) Cycling performance of the NHCS//MPF/C/CeO_2-5 ACS device at 1 A/g current density b) Cycling performance of the NHCS//pristine MPF ACS device at 1 A/g current density, c) Nyquist plots of the NHCS//MPF/C/CeO_2-5 ACS device before and after 15000 cycles, c1) inset showing magnified region of the Nyquist plots for the NHCS//MPF/C/CeO_2-5 ACS device, d) Bode plots of the NHCS//MPF/C/CeO_2-5 ACS device before and after 15000 cycles, and e) Comparative Ragone plot illustrating the performance of the NHCS//MPF/C/CeO_2-5 compared to other Mn-based asymmetric supercapacitors reported in recent literature.

To further understand the electrochemical processes evident in the NHCS//MPF/C/CeO_2-5 device, EIS measurements were performed to determine the interfacial chemical processes. Given the complex surface structure of the MPF/C/CeO_2-5 composite, numerous morphological and structural changes are expected to occur with numerous cycles, and EIS can greatly assist in understanding these processes. Fig. 5c shows the Nyquist plots obtained for the ASC device before (within the first 100 cycles) and after 15 000 cycles with the modelled equivalent Randles circuit (see inset) comprising the solution/electrolyte (R_s), solid-electrolyte interface (R_{sei}), interfacial resistance (R_{int}), charge-transfer resistance (R_{ct}) resulting from electron transport, and double-layer capacitance (C_{dl}). As was evident in the three-electrode studies, two constant phase elements (CPE) corresponding to charge-transfer processes (CPE_{ct}) and the solid-electrolyte interface (CPE_{sei}) were also modelled in the circuit. The modelled parameters are listed in Table 1. The value of R_s increased slightly after 15 000 cycles, which was attributed to the recrystallization of the high-concentration electrolyte. The values of both R_{ct} and R_{sei} decreased after 15 000 cycles, suggesting some activation of the SEI layer, resulting in increased conductivity. R_{int} increased significantly after prolonged cycling, suggesting that diffusion-controlled processes occurring at the interfacial regions become more sluggish over time, potentially due to the formation of unwanted by-products or collapse of the structure, leading to the passivation of active sites at these interfaces. Furthermore, the value of

Table 1
EIS parameters for the 2-electrode asymmetric device.

EIS parameters	NHCS//MPF/C/CeO_2-5 ACS	
	Before 15 000 cycles	After 15 000 cycles
R_s/Ω	1.09 ± 0.23	1.54 ± 0.16
R_{ct}/Ω	6.04 ± 0.76	5.34 ± 0.65
R_{sei} (Ω)	1.29 ± 0.42	0.28 ± 0.05
R_{int} (Ω)	4454 ± 598.30	6773 ± 103.70
C_{dl} (μF)	31.17 ± 1.42	104.40 ± 0.04
CPE_{sei}/mF. $s^{\wedge(a-1)}$	2.14 ± 0.01	0.30 ± 0.09
a	0.50	0.63
CPE_{ct}/mF. $s^{\wedge(a-1)}$	19.73 ± 6.61	15.16 ± 8.47
a	0.91	0.89
f_o/Hz	57.01	84.49
τ/ms	17.54	11.84
Phase angle	−77°	−78°

C_{dl} increased slightly, which suggests that surface-controlled kinetics are enhanced, likely resulting from the inability of the charged species to undergo Faradaic processes or as a result of the contribution of these processes from the CeO_2 coating. Given that the combined resistance values are greater after 15 000 cycles despite the device maintaining favourable performance, this suggests that the device is more diffusion-controlled at the start of its life. Over time, the surface species undergo

irreversible chemical changes and become passivated resulting in sluggish diffusion-controlled kinetics. This suggestion is somewhat supported by observing that the "a" value for CPE_{sei} increases from 0.50 to 0.63, suggesting that there is some purely resistive component evident in the SEI which later becomes more pseudocapacitive, perhaps due to the promotion of charge-separation processes as compared to diffusion processes. The "a" value of CPE_{ct} only displayed a slight decrease from 0.91 to 0.89 after 15 000 cycles, which again suggests a mixed mechanism of pseudocapacitive behavior is evident in the device. The "a" value being close to 1 however suggests that EDLC type behavior predominates in this mixed mechanism, which is likely the cause of the excellent stability of the NHCS//MPF/C/CeO_2-5 device as compared to the NHCS//pristine MPF device. To better understand the power capability of the device using EIS data, the knee frequency (f_o) [62] was investigated before and after 15 000 cycles. A large value of f_o generally indicates a high-power system that can withstand high bursts of energy both inside and outside of the system (i.e., rapid charge and discharge). It is noted that f_o increases from 57.01 Hz to 84.49 Hz after 15 000 cycles, with a decreased response time, τ, from 17.54 ms to 11.84 ms respectively. This result suggests, that indeed, the NHCS//MPF/C/CeO_2-5 device is a high-power system, and its electrochemical performance is enhanced with prolonged use, suggesting further activation of the composite material over time. The slight decrease in the response time also indicated an enhancement in the devices performance. Furthermore, the phase angle obtained from the Bode plots (Fig. 5d) remained almost constant before (−77°) and after (−78°) 15 000 cycles despite the changes f_o and τ which further indicates the impressive stability of the device. Fig. 5e shows the Ragone plot of the NHCS//MPF/C/CeO_2-5 device and other manganese-based systems reported in recent literature. The device achieved a maximum specific energy density (E_d) of 21.0 Wh/kg at a specific power density (P_d) of 390.9 W/kg at a current density of 0.1 A/g. At a current density of 3 A/g, the device achieved a remarkable P_d of 11 632 W/kg while retaining an E_d of 11.2 Wh/kg.

Compared with other recently reported manganese-based materials used in ASC devices, the NHCS//MPF/C/CeO_2-5 device displays favourable P_d, albeit with poorer E_d, compared to manganese phosphate based systems such as those presented in Table S5 [63–70]. It should be noted that the E_d of the NHCS//MPF/C/CeO_2-5 device is seemingly better than those reported here, however, the E_d of our device is reported at a considerably lower current density (0.1 A/g) than the other manganese-based systems listed, however, the device still retains a greater energy density at higher current densities compared to the AC//$Mn_3(PO_4)_2$/GF [64], AC//$NaMnPO_4$[65], and AC//PANI-$Mn_3(PO_4)_2$[66] manganese phosphate systems. Furthermore, in comparison to all the managanese-based systems listed, the NHCS//MPF/C/CeO_2-5 device has superior P_d at considerably lower current densities when compared to the other devices. Table S6 provides a further comparison between the parameters of the NHCS//MPF/C/CeO_2-5 device and the other manganese-based systems presented in Table S5. Notably, the NHCS//MPF/C/CeO_2-5 device displays comparable or improved capacity retention compared to the other Mn-based devices reported after 15 000 cycles, with the highest number of cycles reported from these sources being 10 000 cycles. Furthermore, the sources reporting a higher capacity retention have either been through a lower number of cycles or were cycled at higher current densities. At higher current densities, diffusion-controlled kinetics which are generally responsible for chemical changes which lead to capacity fading are limited, and thus capacity retention is expected to be maintained better than when cycled at lower current densities. These comparisons confirm that the NHCS//MPF/C/CeO_2-5 device is a remarkably stable, high-power system as previously suggested from electrochemical studies. This result suggests that MPF/C/CeO_2-5 is a suitable candidate to consider for high power applications, and highlights the effect of CeO_2 on the overall stability of pristine MPF.

4. Conclusion

In summary, the viability of using triplite Mn_2PO_4F as an electrode material in asymmetric supercapacitors was explored. Pristine MPF was successfully synthesised using a microwave-assisted method and coated with 2.5 wt%, 5 wt%, and 7.5 wt% of CeO_2 to investigate the effect of the coatings on the overall performance and stability of MPF. A 10 wt% carbon black coating was introduced as a conducting agent. The as-synthesised materials were physically and electrochemically characterized to evaluate the performance of the pristine MPF and the effects of the addition of CeO_2/CB coatings. Three-electrode investigations in a 17 m $NaClO_4$ WIS electrolyte concluded that a 5 % CeO_2 coating is most optimal for enhancing the performance of pristine MPF. A two-electrode asymmetric supercapacitor full cell was assembled with MPF/C/CeO_2-5 as the positive electrode and NHCS as the negative electrode. The NHCS//MPF/C/CeO_2-5 device obtained a maximum specific capacitance of 38 F/g at a current density of 0.1 A/g in the same WIS electrolyte used for three-electrode studies. At a current density of 0.1 A/g the device achieved a maximum energy density of 21.0 Wh/kg at a power density of 390.9 W/kg, which shows some improvement compared to other manganese phosphate-based materials reported in recent literature for similar applications. At a current density of 3 A/g the device displayed favourable characteristics for a high-power system, achieving an impressive power density of 11 632 W/kg at an energy density of 11.2 Wh/kg. This result is promising, considering that other manganese-based materials achieve similar power densities only at higher current densities. Furthermore, cycling stability studies showed that the NHCS//MPF/C/CeO_2-5 device achieved an 89.0 % capacity retention after 15 000 cycles at a 1 A/g current density, which is a significant improvement to a NHCS//pristine MPF device, which achieved only 64.9 % capacity retention after a similar study. This result confirms that CeO_2 significantly improves the rate capability and cyclic stability of the pristine MPF. This improvement in stability is suspected to result from variation in the content of Mn^{2+} and Mn^{3+} species, and perhaps oxygen vacancies, as highlighted by XPS analysis. Further investigation of the content of these species, as well as the possibility of effects such as Jahn-Teller distortion and disproportionation reactions, may provide useful insights into the observed trends in the performance and stability of the materials with varying CeO_2 content. These findings contribute to the development of interest in the study of fluorophosphate materials in electrochemical systems and conclude that MPF/C/CeO_2-5 is a promising candidate for high-power applications requiring rapid charge/discharge rates.

CRediT authorship contribution statement

Ryan O'Connor: Writing – original draft, Methodology, Investigation, Formal analysis, Data curation. **Thapelo P. Mofokeng:** Writing – original draft, Data curation. **Aderemi B. Haruna:** Writing – review & editing, Writing – original draft, Methodology, Investigation, Data curation, Conceptualization. **Maxwell W. Terban:** Writing – review & editing, Formal analysis, Data curation. **Dean H. Barrett:** Writing – review & editing, Supervision, Formal analysis, Data curation. **Kenneth I. Ozoemena:** Writing – review & editing, Supervision, Resources, Project administration, Funding acquisition, Conceptualization.

Declaration of competing interest

The authors declare that they have no known competing financial interests or personal relationships that could have appeared to influence the work reported in this paper.

Acknowledgments

The authors are grateful for the financial support of the National Foundation of Research (NRF), the Department of Science and

Innovation (DSI) Energy Storage Consortium, and the DSI-NRF-Wits SARChI Chair in Materials Electrochemistry and Energy Technologies (MEET) (UID no.: 132739); Doctoral scholarship awarded by the South African National Research Foundation (Grant no. PMDS22060719754). The acquisition of synchrotron data was also funded through the South Africa National Research Foundation (Grant no. SRUG2204041774). We acknowledge the European Synchrotron Radiation Facility (ESRF) for providing synchrotron radiation facilities under proposal MA5435 and the Canadian Light Source under proposals 36G12674 and 37G12950. We would like to thank Dr Beatriz Moreno for her assistance in collecting the synchrotron data.

Appendix A. Supplementary data

Supplementary data to this article can be found online at https://doi.org/10.1016/j.jpowsour.2024.236081.

Data availability

Data will be made available on request.

References

[1] T. Kim, S. Subedi, B. Dahal, K. Chhetri, T. Mukhiya, A. Muthurasu, J. Gautam, P. C. Lohani, D. Acharya, I. Pathak, S.H. Chae, T.H. Ko, H.Y. Kim, Adv. Sci. 9 (2022) 1–11, https://doi.org/10.1002/advs.202200650.
[2] X. Xiao, T. Li, Z. Peng, H. Jin, Q. Zhong, Q. Hu, B. Yao, Q. Luo, C. Zhang, L. Gong, J. Chen, Y. Gogotsi, J. Zhou, Nano Energy 6 (2014) 1–9, https://doi.org/10.1016/j.nanoen.2014.02.014.
[3] Y. Shao, M.F. El-Kady, J. Sun, Y. Li, Q. Zhang, M. Zhu, H. Wang, B. Dunn, R. B. Kaner, Chem. Rev. 118 (2018) 9233–9280, https://doi.org/10.1021/acs.chemrev.8b00252.
[4] K. Makgopa, P.M. Ejikeme, C.J. Jafta, K. Raju, M. Zeiger, V. Presser, K.I. Ozoemena, J. Mater. Chem. A 3 (2015) 3480–3490, https://doi.org/10.1039/C4TA06715K.
[5] J. Cao, Y. Wang, Y. Zhou, J.H. Ouyang, D. Jia, L. Guo, J. Electroanal. Chem. 689 (2013) 201–206, https://doi.org/10.1016/j.jelechem.2012.10.024.
[6] P. Barpanda, L. Lander, S.I. Nishimura, A. Yamada, Adv. Energy Mater. 8 (2018) 1–26, https://doi.org/10.1002/aenm.201703055.
[7] C. Masquelier, L. Croguennec, Chem. Rev. 113 (2013) 6552–6591, https://doi.org/10.1021/cr3001862.
[8] R.K.B. Gover, P. Burns, A. Bryan, M.Y. Saidi, J.L. Swoyer, J. Barker, Solid State Ionics 177 (2006) 2635–2638, https://doi.org/10.1016/j.ssi.2006.04.049.
[9] N.R. Khasanova, O.A. Drozhzhin, D.A. Storozhilova, C. Delmas, E.V. Antipov, Chem. Mater. 24 (2012) 4271–4273, https://doi.org/10.1021/cm302724a.
[10] J. Barker, R.K.B. Gover, P. Burns, A. Bryan, M.Y. Saidi, J.L. Swoyer, J. Power Sources 146 (2005) 516–520, https://doi.org/10.1016/j.jpowsour.2005.03.126.
[11] L. Sharma, S.P. Adiga, H.N. Alshareef, P. Barpanda, Adv. Energy Mater. 10 (2020) 1–27, https://doi.org/10.1002/aenm.202001449.
[12] J.R. Rea, E. Kostiner, Acta Crystallogr. Sect. B Struct. Crystallogr. Cryst. Chem. 28 (1972) 2525–2529, https://doi.org/10.1107/s0567740872006417.
[13] Z. Zhang, W. Li, Y. Shen, R. Wang, H. Li, M. Zhou, W. Wang, K. Wang, K. Jiang, J. Energy Storage 45 (2022) 103729, https://doi.org/10.1016/j.est.2021.103729.
[14] M.N. Sakib, S. Ahmed, S.M.S.M. Rahat, S.B. Shuchi, J. Energy Storage 44 (2021) 103322, https://doi.org/10.1016/j.est.2021.103322.
[15] R. Hurman Eric, Miner. Process. Extr. Metall. Rev. 15 (1995) 191–200, https://doi.org/10.1080/08827509508914197.
[16] N. Nzimande, A. Haruna, P. Mwonga, B. Rasche, F. Cummings, K.I. Ozoemena, ACS Appl. Energy Mater. 4 (2021) 13085–13097, https://doi.org/10.1021/acsaem.1c02734.
[17] C.E. Castano, M.J. O'Keefe, W.G. Fahrenholtz, Curr. Opin. Solid State Mater. Sci. 19 (2015) 69–76, https://doi.org/10.1016/j.cossms.2014.11.005.
[18] S. Hao, D. Zhang, Y. Li, X. Xi, S. Wang, X. Li, X. Shen, S. Liu, J. Zheng, Nanoscale 13 (2021) 20213–20224, https://doi.org/10.1039/d1nr05912b.
[19] Y. Liu, C. Mi, C. Yuan, X. Zhang, J. Electroanal. Chem. 628 (2009) 73–80, https://doi.org/10.1016/j.jelechem.2009.01.008.
[20] J. Yao, F. Wu, X. Qiu, N. Li, Y. Su, Electrochim. Acta 56 (2011) 5587–5592, https://doi.org/10.1016/j.electacta.2011.03.141.
[21] Q. Huang, C. Qian, C. Liu, Y. Chen, J. Colloid Interface Sci. 654 (2024) 626–638, https://doi.org/10.1016/j.jcis.2023.10.075.
[22] R.L. Patel, S.A. Palaparty, X. Liang, J. Electrochem. Soc. 164 (2017) A6236–A6243, https://doi.org/10.1149/2.0371701jes.
[23] K. Liu, G.L. Yang, Y. Dong, T. Shi, L. Chen, J. Power Sources 281 (2015) 370–377, https://doi.org/10.1016/j.jpowsour.2014.12.131.
[24] H. Gao, K. Tang, J. Xiao, X. Guo, W. Chen, H. Liu, G. Wang, J. Energy Chem. 69 (2022) 84–99, https://doi.org/10.1016/j.jechem.2021.12.025.
[25] X. Tian, Q. Zhu, B. Xu, ChemSusChem 14 (2021) 2501–2515, https://doi.org/10.1002/cssc.202100230.
[26] J. Cai, Y. Ding, R. Bai, C. Zhang, X. Zhang, H. Sun, G. Wang, J. Colloid Interface Sci. 651 (2023) 534–543, https://doi.org/10.1016/j.jcis.2023.08.015.
[27] A.F.G. Leontowich, A. Gomez, B.D. Moreno, D. Muir, D. Spasyuk, G. King, J. W. Reid, C.-Y. Kim, S. Kycia, J. Synchrotron Radiat. 28 (2021) 961–969, https://doi.org/10.1107/S1600577521002496.
[28] A.A. Coelho, J. Appl. Crystallogr. 51 (2018) 210–218, https://doi.org/10.1107/S1600576718000183.
[29] P. Juhás, T. Davis, C.L. Farrow, S.J.L. Billinge, J. Appl. Crystallogr. 46 (2013) 560–566, https://doi.org/10.1107/S0021889813005190.
[30] X. Yang, P. Juhas, C. L. Farrow and S. J. L. Billinge, 2014, doi: 10.48550/arXiv.1402.3163..
[31] C.L. Farrow, P. Juhas, J.W. Liu, D. Bryndin, E.S. Bozin, J. Bloch, T. Proffen, S.J. L. Billinge, J. Phys. Condens. Matter 19 (2007) 335219, https://doi.org/10.1088/0953-8984/19/33/335219.
[32] J. Lee, N. Jäckel, D. Kim, M. Widmaier, S. Sathyamoorthi, P. Srimuk, C. Kim, S. Fleischmann, M. Zeiger, V. Presser, Electrochim. Acta 222 (2016) 1800–1805, https://doi.org/10.1016/j.electacta.2016.11.148.
[33] P.W. Ruch, D. Cericola, M. Hahn, R. Kötz, A. Wokaun, J. Electroanal. Chem. 636 (2009) 128–131, https://doi.org/10.1016/j.jelechem.2009.09.007.
[34] S. Roldán, D. Barreda, M. Granda, R. Menéndez, R. Santamaría, C. Blanco, Phys. Chem. Chem. Phys. 17 (2015) 1084–1092, https://doi.org/10.1039/c4cp05124f.
[35] T.P. Mofokeng, A.K. Ipadeola, Z.N. Tetana, K.I. Ozoemena, ACS Omega 5 (2020) 20461–20472, https://doi.org/10.1021/acsomega.0c02563.
[36] H.W. Nesbitt, D. Banerjee, Am. Mineral. 83 (1998) 305–315, https://doi.org/10.2138/am-1998-3-414.
[37] B. Sambandam, V. Mathew, S. Kim, S. Lee, S. Kim, J.Y. Hwang, H.J. Fan, J. Kim, Chem 8 (2022) 924–946, https://doi.org/10.1016/j.chempr.2022.03.019.
[38] Z. Xiao, F. Xia, L. Xu, X. Wang, J. Meng, H. Wang, X. Zhang, L. Geng, J. Wu, L. Mai, Adv. Funct. Mater. 32 (2022) 1–9, https://doi.org/10.1002/adfm.202108244.
[39] Y. Liu, C. Wang, S. Zhao, L. Zhang, K. Zhang, F. Li, J. Chen, Chem. Sci. 12 (2021) 1062–1067, https://doi.org/10.1039/d0sc05427e.
[40] A.O.O. Bahdad, Y. Li, T. Van Nguyen, J. Electrochem. Soc. 168 (2021) 070524, https://doi.org/10.1149/1945-7111/ac0e4e.
[41] R. Roy, R. Greeshma, P. Dutta, I. Mondal, R. Banerjee, A.K. Singh, ACS Appl. Mater. Interfaces (2024), https://doi.org/10.1021/acsami.4c04445.
[42] H. Lv, Y. Song, Z. Qin, M. Zhang, D. Yang, Q. Pan, Z. Wang, X. Mu, J. Meng, X. Sun, X.X. Liu, Chem. Eng. J. 430 (2022), https://doi.org/10.1016/j.cej.2021.133064.
[43] Y. Son, D.T. Nguyen, Y. Lee, J. Power Sources 533 (2022) 231395, https://doi.org/10.1016/j.jpowsour.2022.231395.
[44] Z. Yang, J. Lv, H. Pang, W. Yan, K. Qian, T. Guo, Z. Guo, Sci. Rep. 5 (2015) 1–10, https://doi.org/10.1038/srep17473.
[45] T.J. Frankcombe, Y. Liu, Chem. Mater. 35 (2023) 5468–5474, https://doi.org/10.1021/acs.chemmater.3c00801.
[46] Z.K. Tang, Y.F. Xue, G. Teobaldi, L.M. Liu, Nanoscale Horizons 5 (2020) 1453–1466, https://doi.org/10.1039/d0nh00340a.
[47] A. Paul, S. Ghosh, H. Kolya, C.W. Kang, N.C. Murmu, T. Kuila, J. Energy Storage 62 (2023) 106922, https://doi.org/10.1016/j.est.2023.106922.
[48] Z.L. Chen, Y.J. Gu, Y.L. Huo, X.Y. Ma, F.Z. Wu, J. Alloys Compd. 917 (2022) 165485, https://doi.org/10.1016/j.jallcom.2022.165485.
[49] J.R. Ebner, D.L. McFadden, R.A. Walton, J. Solid State Chem. 17 (1976) 447–449, https://doi.org/10.1016/S0022-4596(76)80016-3.
[50] V. Davydov, A. Rakhmanina, I. Kireev, I. Alieva, O. Zhironkina, O. Strelkova, V. Dianova, T.D. Samani, K. Mireles, L.H. Yahia, R. Uzbekov, V. Agafonov, V. Khabashesku, J. Mater. Chem. B 2 (2014) 4250–4261, https://doi.org/10.1039/c3tb21599g.
[51] P. Burroughs, A. Hamnett, A. F. Orchard and G. Thornton, J.C.S. Dalt., 1976, 1686–1698..
[52] E. Paparazzo, J. Phys. Condens. Matter 32 (2020) 099501, https://doi.org/10.1088/1361-648x/ab5763.
[53] S.M. Gateman, O. Gharbi, H. Gomes de Melo, K. Ngo, M. Turmine, V. Vivier, Curr. Opin. Electrochem. 36 (2022) 101133, https://doi.org/10.1016/j.coelec.2022.101133.
[54] S.A. Melchior, K. Raju, I.S. Ike, R.M. Erasmus, G. Kabongo, I. Sigalas, S.E. Iyuke, K. I. Ozoemena, J. Electrochem. Soc. 165 (2018) A501–A511, https://doi.org/10.1149/2.0401803jes.
[55] B. Ranjan, D. Kaur, Small (2023) 2307723, https://doi.org/10.1002/smll.202307723, 1–17.
[56] J.S. Ko, C.H. Lai, J.W. Long, D.R. Rolison, B. Dunn, J. Nelson Weker, ACS Appl. Mater. Interfaces 12 (2020) 14071–14078, https://doi.org/10.1021/acsami.0c02020.
[57] J. Wang, J. Polleux, J. Lim, B. Dunn, J. Phys. Chem. C 111 (2007) 14925–14931, https://doi.org/10.1021/jp074464w.
[58] T.-C. Liu, W.G. Pell, B.E. Conway, S.L. Roberson, J. Electrochem. Soc. 145 (1998) 1882–1888, https://doi.org/10.1149/1.1838571.
[59] T.P. Mofokeng, Z.N. Tetana, K.I. Ozoemena, Carbon N. Y. 169 (2020) 312–326, https://doi.org/10.1016/j.carbon.2020.07.049.
[60] T. Brezesinski, J. Wang, S.H. Tolbert, B. Dunn, Nat. Mater. 9 (2010) 146–151, https://doi.org/10.1038/nmat2612.
[61] V. Shrivastav, Mansi, P. Dubey, V. Shrivastav, A. Kaur, M. Hołdyński, A. Krawczyńska, U.K. Tiwari, A. Deep, W. Nogala, S. Sundriyal, Sci. Rep. 13 (2023) 1–14, https://doi.org/10.1038/s41598-023-47730-4.
[62] C. Du, N. Pan, J. Power Sources 160 (2006) 1487–1494, https://doi.org/10.1016/j.jpowsour.2006.02.092.
[63] X. Bu, Y. Zhang, L. Su, Q. Dou, Y. Xue, X. Lu, Ionics 25 (2019) 6007–6015, https://doi.org/10.1007/s11581-019-03141-y.
[64] K.O. Oyedotun, T.M. Masikhwa, A.A. Mirghni, B.K. Mutuma, N. Manyala, Electrochim. Acta 334 (2020) 135610, https://doi.org/10.1016/j.electacta.2020.135610.

[65] A. Chowdhury, S. Biswas, A. Dhar, P.S. Burada, A. Chandra, J. Power Sources 516 (2021) 230679, https://doi.org/10.1016/j.jpowsour.2021.230679.
[66] C.C. Lee, F.S. Omar, A. Numan, N. Duraisamy, K. Ramesh, S. Ramesh, J. Solid State Electrochem. (2017) 3205–3213, https://doi.org/10.1007/s10008-017-3624-1.
[67] Y. Zhu, H. Chen, S. Chen, C. Li, M. Fan, K. Shu, J. Mater. Sci. 53 (2018) 6157–6169, https://doi.org/10.1007/s10853-017-1976-7.
[68] G.P. Ojha, A. Muthurasu, B. Dahal, T. Mukhiya, D. Kang, H.Y. Kim, J. Electroanal. Chem. 837 (2019) 254–265, https://doi.org/10.1016/j.jelechem.2019.02.021.
[69] M. Karuppaiah, R. Akilan, P. Sakthivel, S. Asaithambi, R. Shankar, R. Yuvakkumar, Y. Hayakawa, G. Ravi, J. Energy Storage 27 (2020) 101138, https://doi.org/10.1016/j.est.2019.101138.
[70] S. Shi, G. Wan, L. Wu, Z. He, K. Wang, Y. Tang, X. Xu, G. Wang, J. Colloid Interface Sci. 537 (2019) 142–150, https://doi.org/10.1016/j.jcis.2018.11.006.